JGR Solid Earth

RESEARCH ARTICLE
10.1029/2020JB021137

An Alternative Approach for Constraining 3D-Displacements With InSAR, Applied to a Fault-Bounded Groundwater Entrainment Field in California

K. D. Murray[1], R. B. Lohman[2], J. Kim[3], and W. E. Holt[3]

[1]Department of Earth Sciences, University of Hawaii at Manoa, Honolulu, HI, USA, [2]Department of Earth and Atmospheric Sciences, Cornell University, Ithaca, NY, USA, [3]Department of Geosciences, Stony Brook University, Stony Brook, NY, USA

Key Points:

- In 2017, upto 12 cm of line-of-sight (LOS) displacement occurred at the Whitewater groundwater entrainment site
- We compare methods for inferring 3-D velocities from 1-D interferometric synthetic aperture radar (InSAR) measurements
- The Garnet Hill Fault experienced increased right-lateral sense of shear in some areas

Supporting Information:

Supporting Information may be found in the online version of this article.

Correspondence to:

K. D. Murray,
murray8@hawaii.edu

Citation:

Murray, K. D., Lohman, R. B., Kim, J., & Holt, W. E. (2021). An alternative approach for constraining 3D-displacements with InSAR, applied to a fault-bounded groundwater entrainment field in California. *Journal of Geophysical Research: Solid Earth*, *126*, e2020JB021137. https://doi.org/10.1029/2020JB021137

Received 6 OCT 2020
Accepted 2 APR 2021

Abstract We explore the use of elastic Green's functions in inversions of one-dimensional Interferometric Synthetic Aperture Radar (InSAR) observations to recover three-dimensional displacement fields. This approach enforces coupling of the horizontal displacements and limits the need for prior assumptions about the subsurface sources, driving the deformation or explicit damping of a given dimension of the full 3D deformation field. We apply these methods to data from the Coachella Valley, California, where artificial groundwater recharge in 2017 and the associated increases in pore pressure resulted in ground displacements of up to 12 cm. This area is covered by Sentinel-1a/b data for two overlapping paths from both ascending and descending orbits, as well as an east-west flight line from the Uninhabited Aerial Vehicle Synthetic Aperture Radar (UAVSAR), providing five unique line-of-sight geometries. The regularization approaches applied to the Sentinel data alone agree in most respects, with the elastically coupled approach producing a slightly better fit to the independent UAVSAR observations. Our results suggest that the 2017 groundwater entrainment in the Coachella Valley is likely associated with significant horizontal displacements that led to contraction across the fault bounding the northern side of the basin, as well as increases in right-lateral sense of strain in some areas along the fault.

1. Introduction

Interferometric Synthetic Aperture Radar (InSAR) observations constrain displacement of the Earth's surface toward or away from the satellite, and are inherently a one-dimensional observation defined by the projection of the true, 3-dimensional (3-D) ground displacement field onto the orientation of the line-of-sight (LOS) vector between the satellite and the ground (e.g., Bürgmann et al., 2000). However, interpretations of the deformation within a given region usually benefit from constraints on the full 3-D displacement field (e.g., Fialko et al., 2001; Funning et al., 2005; Wright et al., 2004) or require well-characterized physical models of the processes driving the deformation (e.g., fault source geometry, aquifer characteristics, crustal rigidity). These models are not always available or well understood and the Earth is far more complex in reality than its representation in models (e.g., Caricchi et al., 2014; Chester & Chester, 2000; Hearn & Bürgmann, 2005). To address this limitation, researchers have combined measurements from multiple observation geometries (particularly from ascending and descending satellite paths) as well as other products derived from the Synthetic Aperture Radar (SAR) imagery (described below) to infer the 3-D displacement field and its variations over time (e.g., Fialko, 2004; Froger et al., 2004; Funning et al., 2005; Joughin et al., 1998; Lindsey et al., 2014; Samieie-Esfahany et al., 2009). Although these combinations provide some separation of east-west and vertical components, the north-south direction often remains poorly resolved due to the polar orbits of SAR satellites. The NASA/JPL Uninhabited Aerial Vehicle Synthetic Aperture Radar (UAVSAR) (Rosen et al., 2006) may be used to improve north-south constraints (e.g., Delbridge et al., 2016; Handwerger et al., 2019), although global data coverage remains sparse both spatially and temporally.

Previous studies have shown that constraints on the full 3-D displacement field can be achieved through analysis of other aspects of the SAR imagery, including the backscatter amplitude and finite beamwidth used in imaging. Cross-correlation of the backscatter amplitude between two different images results in constraints on displacement along the direction of the satellite track, and is useful for measuring signals

with large offsets greater than ~10% of the pixel size (e.g., Fialko et al., 2001, 2005; Grandin et al., 2016; Hu et al., 2010; Jiang et al., 2017; Jónsson et al., 2002; Michel et al., 1999; Simons et al., 2002). Split-beam methods, known as multiple aperture radar (MAI) or "burst overlap interferometry" for Sentinel-1 TOPS mode, have been employed to constrain along-track displacements (Bechor & Zebker, 2006; Grandin et al., 2016; Gray, 2011; J. Hu et al., 2012; Jung et al., 2012). This method uses subaperture processing in the azimuth direction to separate an interferogram into forward- and backward-looking components. MAI and burst-overlap approaches improve precision relative to amplitude cross-correlation, but still can only constrain relatively large signals (typically >~5 cm) (e.g., Grandin et al., 2016; Jiang et al., 2017). Moreover, burst overlap interferometry can only be done in the areas where bursts or swaths overlap.

Given the limited viewing geometries available from satellite-based systems and the limitations on amplitude cross-correlation and split-beam methods, how can we best leverage the high precision of LOS-phase changes and infer characteristics of the 3-D displacement field? To answer this question we propose a method that incorporates elastic Green's functions as constraints on the displacement gradients in each dimension, an approach that has already been explored for use in interpolating spatially smooth signals in sparse GPS data (e.g., Haines et al., 2015; Sandwell & Wessel, 2016). We test our approach on a site of groundwater entrainment in the Coachella Valley in southern California.

Both natural and anthropogenic changes in storage and flow of groundwater and other subsurface fluids can impact the effective stress on faults. This can happen through an increase in pore pressure at the fault interface and lead to fault slip and elevated seismicity (e.g., Ellsworth, 2013; Keranen & Weingarten, 2018; Ross et al., 2020; Savage et al., 2017; Wetzler et al., 2019), or through stress changes related to poroelastic deformation or loading (e.g., González et al., 2012; Johnson et al., 2017; Hu & Bürgmann, 2020; Segall, 1989). In some cases, these poroelastic changes in the subsurface can lead to deformation at the Earth's surface which can be measured using geodetic methods such as InSAR. In this study, we use InSAR measurements to examine deformation related to anthropogenic groundwater recharge in the Coachella Valley in California. We show that the inferred strain along nearby faults depends on the approach used in reconstructing the 3-D surface displacements.

In Section 2, we describe the general problem setup for inversions for 3-D displacements from InSAR and in Section 3, we describe the data set used in our study. In Section 4, we describe our regularization approach and apply it to synthetic case examples. Section 5 includes our results for the Coachella Valley data and discussion of the potential implications for faults in the vicinity of the entrainment site, followed by conclusions in Section 6.

2. Whitewater Subbasin Case Study

2.1. Study Area

The Whitewater River Subbasin (Figure 1) is an area of active groundwater entrainment in the Coachella Valley of southern California. We observe rapid uplift within the sub-basin throughout 2017, which is likely in response to pore pressure increases within the aquifer. During the entrainment process, water is imported from the Sacramento Bay Delta, Colorado River, and San Gorgonio Mountains and percolated directly into the aquifer system as part of an effort to meet demands from domestic and commercial water consumers in the Coachella Valley (District, C. V. W., 2019). The greater Coachella Valley Groundwater Basin spans an area of ~1000 km^2 and is bounded by crystalline bedrock of the Peninsular Ranges to the southwest and Transverse Ranges to the northeast. The boundary of the Whitewater River sub-basin is delineated by two major faults, the Palm Springs blind fault in the southwest and the Garnet Hill fault in the northeast (bold black lines in Figure 1). The main aquifer occupies the upper ~600 m of the ~3,700 m deep sedimentary basin, and is composed of interbedded layers of gravel, sands, silts, and clays (Coachella Valley Water District, C. V. W., 2019). The aquifer is unconfined and water typically flows from the northwest to the southeast down the Salton Trough.

The Whitewater River Sub-basin does not contain any significant aquitard layers, leading to conditions of high permeability and hydraulic conductivity within the aquifer. Thus, any observed deformation associated with changes in the aquifer system is likely due to a poroelastic response from changes in pore pressure

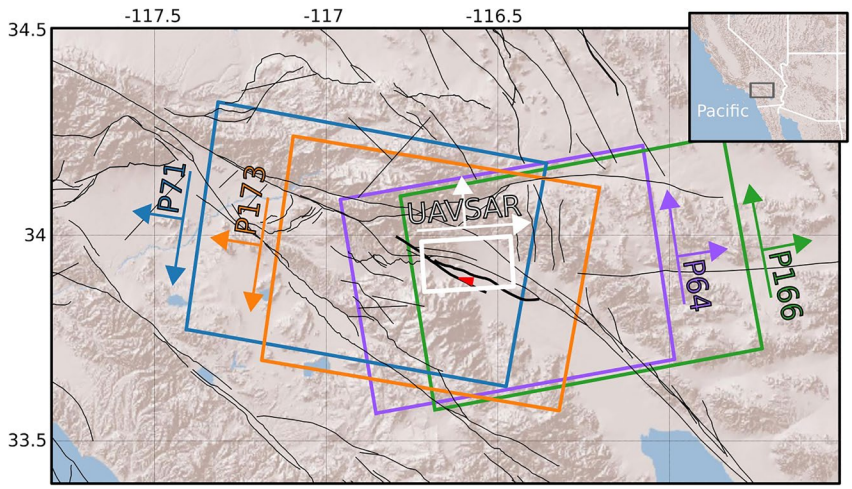

Figure 1. Extent of study area. Colored boxes represent the extent of the four Sentinel-1a/b swaths and Uninhabited Aerial Vehicle Synthetic Aperture Radar (UAVSAR) data (white box) used in this study. The Whitewater groundwater replenishment facility percolation grounds are roughly highlighted with a small red triangle. Faults from the Southern California Earthquake Center (SCEC) Community Fault Model are shown as black lines. Palm Springs blind fault and Garnet Hill fault are indicated with bold black lines. Long arrows indicate satellite flight direction and shorter arrows indicate the look direction.

within the aquifer. In 2017, heavy precipitation relieved a severe 4-year drought in California and resulted in decreased dependence on groundwater pumping and increased deliveries of surface water to areas like the Whitewater groundwater replenishment facility (e.g., Murray & Lohman, 2018). Deliveries to the Whitewater facility increased from essentially zero in 2015 to as much as 400 km^3 in 2017 (Coachella Valley Water District, C. V. W., 2019) and groundwater elevations in nearby wells increased from ~150 m to nearly 240 m over the same time interval (Figure 2).

2.2. InSAR Data

We used Sentinel-1a/b imagery (e.g., De Zan & Monti Guarnieri, 2006) from four overlapping ground tracks as well as observations from the airborne UAVSAR platform to construct displacement time series covering the Whitewater River sub-basin and surrounding area. We processed Sentinel-1 SAR imagery using the InSAR Scientific Computing Environment (ISCE) (Rosen et al., 2012) stack processing capability (Fattahi

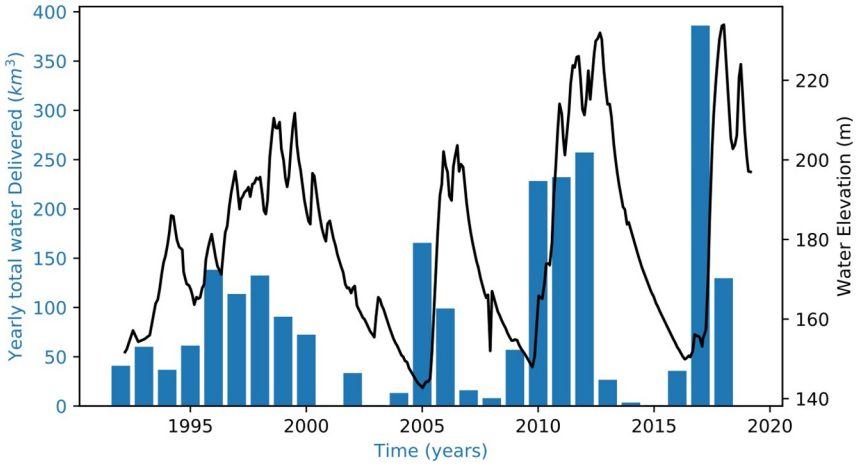

Figure 2. Groundwater elevation (black line) at United States Geological Survey (USGS) well 03S04E20F01S (https://waterdata.usgs.gov/nwis/gw) and yearly total water delivered to the Whitewater groundwater replenishment facility (Coachella Valley Water District, C. V. W., 2019). The location of the well is shown in Figure 3a.

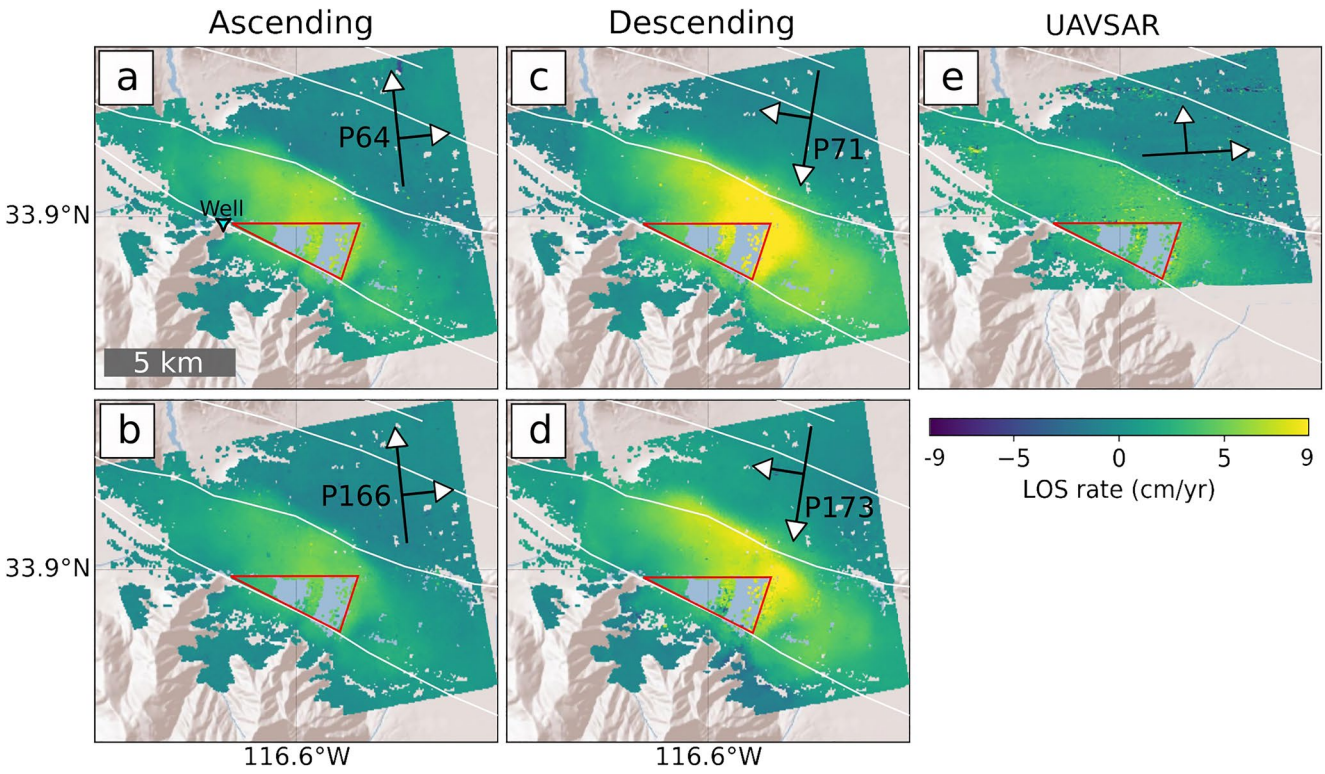

Figure 3. Observed displacement rates during 2017 for the five independent Interferometric Synthetic Aperture Radar (InSAR) datasets. Positive values indicate displacement toward the satellite. Decorrelated areas and high elevation areas (>500 m) have been masked out and are not used in our analysis. The Whitewater groundwater replenishment facility percolation grounds are roughly outlined in red and the USGS well 03S04E20F01S (https://waterdata.usgs.gov/nwis/gw) is labeled in panel (a) (black triangle). Faults from the Southern California Earthquake Center (SCEC) Community Fault Model are shown as white lines. The approximate extent of each panel is outlined by the white box in Figure 1. Rates are constructed using 18 acquisitions from the date range 02/26/2017–11/29/2017 (a), 29 acquisitions from 02/21/2017–12/06/2017 (b), 17 acquisitions from 03/04/2017–12/05/2017 (c), 13 acquisitions from 05/10/2017–12/12/2017 (d), and two acquisitions from 04/04/2017–09/28/2017 (e).

et al., 2016). We generated all sets of sequential interferograms between adjacent dates in individual stacks and used the Shuttle Radar Topography Mission (SRTM) digital elevation model to remove topographic effects (Farr & Kobrick, 2000). Time series were formed using a modified persistent scatter method (Murray & Lohman, 2018). We acquired UAVSAR interferograms from NASA-JPL (Hensley et al., 2009). We removed a long wavelength signal from the UAVSAR interferograms to approximate errors related to flight instabilities. We reference the phase in all interferograms to a relatively stable/coherent location at coordinates 116.528°W, 33.908°N, well north of the area of deformation.

The combination of these InSAR measurements indicate low rates of deformation in 2015 and 2016, rapid uplift in 2017, and variable deformation in 2018 and 2019 (Figures 3 and 4). In the area of maximum deformation we measure ~12 cm of total LOS shortening in 2017 (Figure 4a). The onset of uplift begins north of the entrainment field near the Garnet Hill fault, then progresses outward over the next few months until it extends a small distance (~0.5 km) beyond the mapped extent of the basin-bounding faults to the northeast (Figure 4b). In the southwest, the limit of the observed deformation is more closely related to the transition between the sedimentary basin and bedrock than to the mapped location of the Palm Springs blind fault (Figure 4b). The northeastern limit of deformation closely follows a portion of the mapped location of the Garnet Hill Fault, but then extends to the north by approximately 0.5 km at the northern end of the deforming region.

For the 3-D inversions we use a subset of the Sentinel interferograms to infer the rates during the prominent signal in 2017 (Figure 3) and in the case of UAVSAR we use a single interferogram (04/04/2017–09/28/2017) (Figure 4a, blue diamonds) that spans the main time period of deformation (Figure 3). Due to poor temporal coverage and strong tropospheric turbulence in data from path 173, we omit this path from the inversion

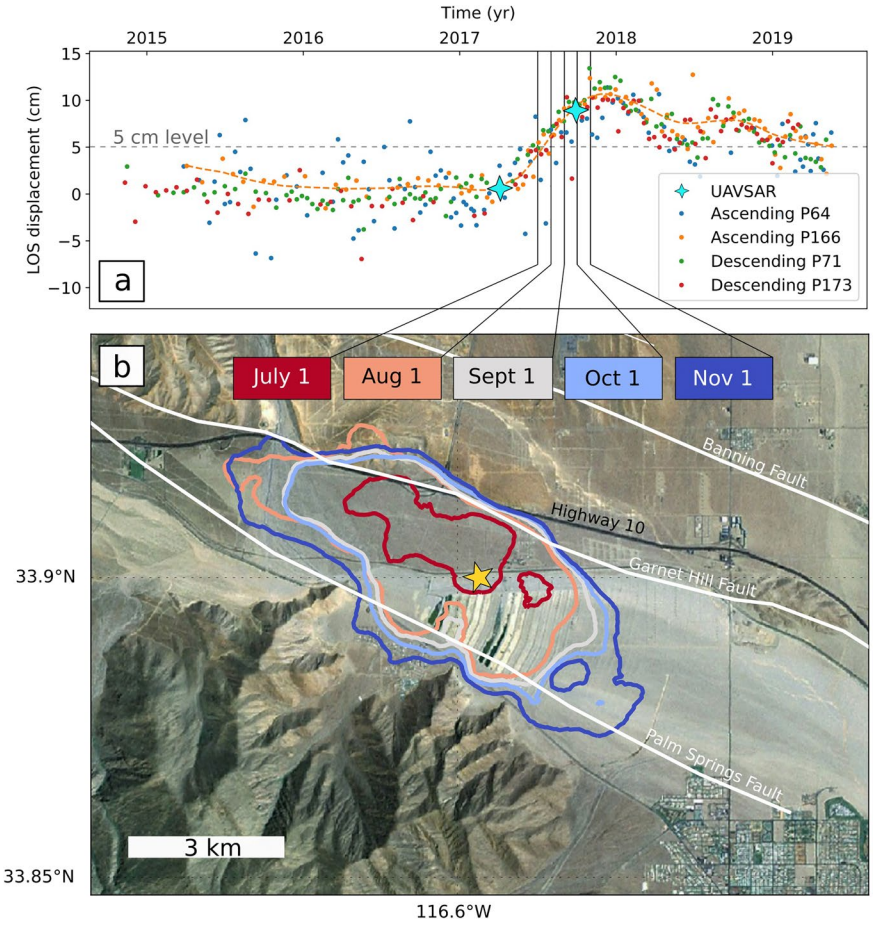

Figure 4. Displacement time series within the Whitewater River Basin and contour map. (a) line-of-sight (LOS) observations from each track are plotted in the time series (location indicated by yellow star in map) with the track P166 data filtered time series plotted (orange dashed line). (b) Timing of uplift, with contours indicating the region where the filtered LOS displacement (from Sentinel-1a/b track P166) exceeds 5 cm (indicated by dashed gray line in time series in [a]) on each date (colors). Faults from the Southern California Earthquake Center (SCEC) Community Fault Model are shown as white lines.

comparisons. We compare the data from path 173 with the predictions from the inferred 3D models in supplementary Figure S1.

2.3. GPS-Based Correction of Interseismic Motion

The study area is located within the region impacted by interseismic motion associated with the Pacific-North American plate boundary. We remove a model of regional displacements from our inferred 3-D displacement fields (presented in Section 5.2) using the UCERF-3 model (Parsons et al., 2013) derived from GPS measurements in the greater region (Figure 5). The magnitude of the correction varies by approximately 0.3 cm/yr between the northeastern and southwestern corners of our study area. This value is only about 3% of the magnitude of maximum horizontal signal related to groundwater entrainment. While not critical to the interpretation of our results, the use of this correction removes the approximately linear ramp in displacement associated with interseismic motion across our study area and helps to isolate the portion of the deformation field associated with hydrology.

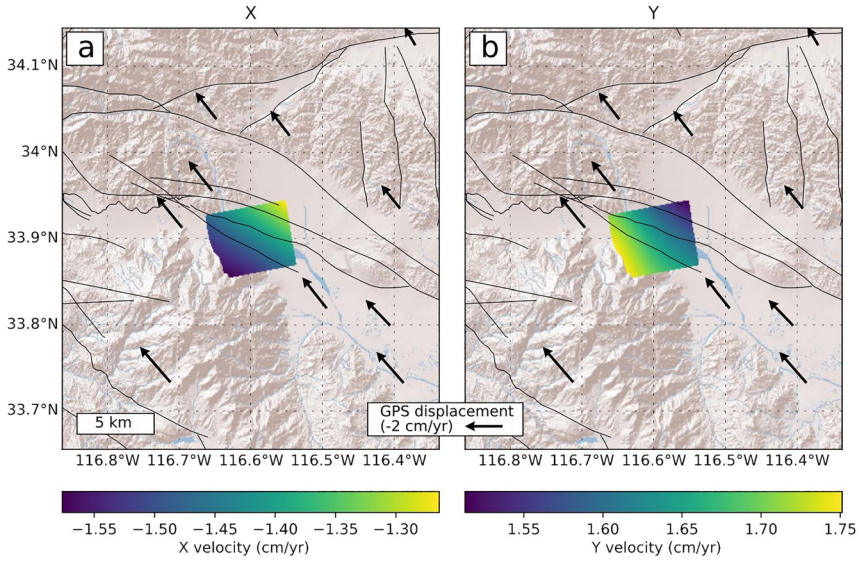

Figure 5. GPS velocities (black vectors) in the NA12 reference frame, available from the Nevada Geodetic Laboratory (http://geodesy.unr.edu). Color scale is UCERF-3: interpolated GPS east velocities (a) and north velocities (b) (Parsons et al., 2013). These velocities were used to subtract motion associated with the plate boundary from Interferometric Synthetic Aperture Radar (InSAR)-derived displacements.

3. Inversion Method for 3-D Decomposition

Our case study and synthetic examples involve a nominally well-determined inversion, where we solve for 3-D displacements based on $N >= 3$ different LOS displacement measurements. Because of the orientation of the LOS vectors, the problem is, in reality, highly unstable, with far less resolution in the N-S direction than in the vertical or E-W direction. The approaches explored here (except for the undamped case) would all be applicable to scenarios with $N = 2$ different LOS as well. For a given pixel, let $\vec{u} = [u_x, u_y, u_z]$ be the actual 3-D displacement vector, with each component corresponding to one of the three orthogonal unit basis vectors $[\hat{i}_x, \hat{i}_y, \hat{i}_z]$. We also consider N unit LOS vectors $\hat{l}_j$ corresponding to each of our satellite viewing geometries. Each of the N LOS geometries at each pixel is a function of the satellite azimuth direction ψ and incidence angle θ (Figure 6) (e.g., Hanssen, 2001):

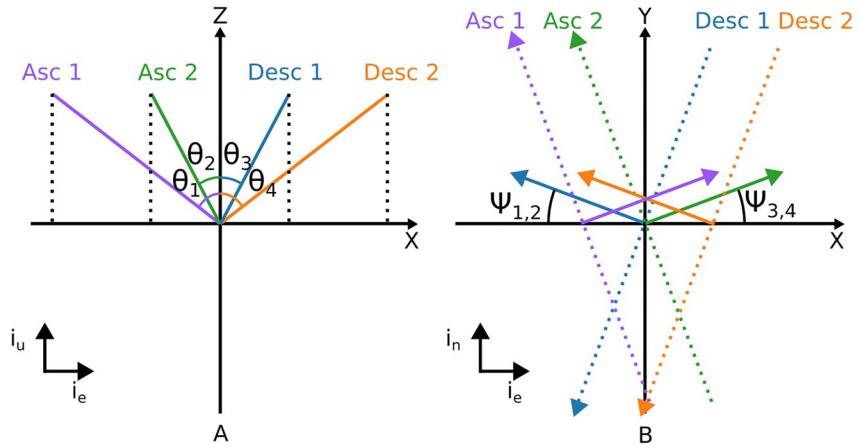

Figure 6. Line-of-sight geometries for the four satellite tracks swaths used in this study in cross section (a) and map view (b), with satellite azimuth direction and incidence angle. Solid lines indicate look vectors for ascending (north-northwest traveling) and descending (south-southwest traveling) tracks (dashed lines). Line colors correspond to colors of footprints in Figure 1.

$$\hat{l}_j = \begin{bmatrix} sin(\theta_j)cos(\psi_j) \\ sin(\theta_j)sin(\psi_j) \\ cos(\theta_j) \end{bmatrix}. \quad (1)$$

The forward problem relating the observations made along the satellite LOS to the 3-D displacement or velocity vector ($\vec{u}$) is

$$\vec{d} = A\vec{u}, \quad (2)$$

where $\vec{d}$ ($N \times 1$) is the vector of observations of LOS displacements, and A ($N \times 3$) is the design matrix:

$$A = \begin{bmatrix} \langle \hat{l}_1, \hat{i}_1 \rangle & \langle \hat{l}_1, \hat{i}_2 \rangle & \langle \hat{l}_1, \hat{i}_3 \rangle \\ \vdots & \vdots & \vdots \\ \langle \hat{l}_N, \hat{i}_1 \rangle & \langle \hat{l}_N, \hat{i}_2 \rangle & \langle \hat{l}_N, \hat{i}_3 \rangle \end{bmatrix}. \quad (3)$$

In the case where $N >= 3$ and the LOS vectors are noncolinear, this problem is not underdetermined and the values of $\vec{u}$ can be inferred as the best-fit solution in a linear least squares sense (e.g., Menke, 2018), as $\vec{u} = (A^T A)^{-1} A^T \vec{d}$. However, when the LOS vectors are near-parallel or clustered within one plane, as they are with most satellite observations, the inverse problem is unstable with respect to small perturbations due to noise in the individual measurements.

Below, we present a regularization method that incorporates constraints from elastic solid mechanics. We compare results from this method to damped least squares solutions, as well as an undamped inversion that incorporates the additional constraints from UAVSAR data.

4. Regularization Approach

4.1. Damped Least Squares Regularization

We implement damped least squares (e.g., Menke, 2018), by augmenting Equation 2 as follows:

$$\begin{bmatrix} \vec{d'} \\ \vec{0} \end{bmatrix} = \begin{bmatrix} A' \\ \lambda^* \end{bmatrix} \vec{u}, \quad (4)$$

where,

$$\lambda^* = \begin{bmatrix} 0 & 0 & 0 \\ 0 & \lambda & 0 \\ 0 & 0 & 0 \end{bmatrix} \quad (5)$$

which is solved in a least squares sense to recover the model vector u. Increasing values of λ will lead to smaller values of u_y, even if the actual values of u_y are large. We find the optimal value for λ through the *jRi* method, which balances the trade-off between perturbation error (noise) and regularization error (over damping) (e.g., Barnhart & Lohman, 2010).

4.2. Elastically Coupled Solution

Haines et al. (2015) developed force-balance equations for the vertical derivatives of horizontal stress rates. These derivatives do not rely on *a priori* assumptions about the subsurface source or material properties. Arbitrary horizontal subsurface forces, f_x and f_y, are related to the horizontal displacement vector $u = [u_x, u_y]$ in the following equations:

$$\left(\frac{2}{1-\nu}\right)\frac{\partial^2 u_x}{\partial x^2}+\left(\frac{2\nu}{1-\nu}\right)\frac{\partial^2 u_y}{\partial x\partial y}+\frac{\partial^2 u_x}{\partial y^2}+\frac{\partial^2 u_y}{\partial x\partial y}=\frac{-f_x}{\mu}\delta(x)\delta(y) \tag{6}$$

$$\frac{\partial^2 u_x}{\partial x\partial y}+\frac{\partial^2 u_y}{\partial x^2}+\left(\frac{2\nu}{1-\nu}\right)\frac{\partial^2 u_x}{\partial x\partial y}+\left(\frac{2}{1-\nu}\right)\frac{\partial^2 u_y}{\partial y^2}=\frac{-f_y}{\mu}\delta(x)\delta(y), \tag{7}$$

where μ is the shear modulus and ν is Poisson's ratio. Sandwell and Wessel (2016) solved Equations 6 and 7 through the frequency domain method involving interpolation of known, arbitrarily spaced measurements of the horizontal component of displacement (e.g., Global Navigation Satellite System [GNSS] data) to a grid of elastically consistent displacement vectors. We modify this approach to regularize our inversion of LOS InSAR measurements to recover a set of elastically consistent horizontal displacement or velocity vectors on the same grid as the InSAR input data. This can also be easily modified to output to an arbitrarily spaced grid. The vertical displacement or velocity vectors are also solved for in this inversion, but without explicit coupling to the horizontal components.

To formulate this linear elastically coupled solution, we solve Equations 6 and 7 according to Sandwell and Wessel (2016) and rewrite the solution with N observations of the 3-D displacement field projected into the LOS as:

$$\begin{bmatrix} \langle \widehat{los_1}, q(\vec{r})+w(\vec{r})\rangle & \langle \widehat{los_1}, w(\vec{r})+p(\vec{r})\rangle & \langle \widehat{los_1}, \hat{i}_3\rangle \\ \vdots & \vdots & \\ \langle \widehat{los_N}, q(\vec{r})+w(\vec{r})\rangle & \langle \widehat{los_N}, w(\vec{r})+p(\vec{r})\rangle & \langle \widehat{los_N}, \hat{i}_3\rangle \end{bmatrix}\begin{bmatrix} f_x \\ f_y \\ u_z \end{bmatrix}=\begin{bmatrix} u_{los1} \\ \vdots \\ u_{losN} \end{bmatrix}, \tag{8}$$

where we have N LOS vectors and the associated set of data vectors, u_{losN}. The Green's functions (q, p, and w) are functions of the vector $\vec{r}=(r_x,r_y)$ which are vectors between each pixel of interest with positions (x_i,y_i) and neighboring pixels with positions (x_j,y_j). $r_x=xi-xj$ and $r_y=y_i-y_j$, and $\vec{r}$ has length $r=\sqrt{r_x^2+r_y^2}$. Following the solution from Sandwell and Wessel (2016), the Green's functions are written as:

$$q(\vec{r})=4\ln r+(1+\nu)\left(\frac{r_y^2}{r^2}-\ln r\right)=(3-\nu)\ln r+(1+\nu)\frac{r_y^2}{r^2} \tag{9}$$

$$p(\vec{r})=(3-\nu)\ln r+(1+\nu)\frac{r_x^2}{r^2} \tag{10}$$

$$w(\vec{r})=-(1+\nu)\frac{r_x r_y}{r^2}. \tag{11}$$

We use a value for Poisson's ratio, ν, of 0.5, which drives the inversion to favor a solution with strong coupling between the horizontal displacements. After inverting Equation 8 for vertical displacements or velocities (u_z) and horizontal forces f_x and f_y in a least squares sense, the forces can be used to recover an elastically consistent set of horizontal displacements u_x and u_y in the forward problem:

$$\begin{bmatrix} u_x^i \\ u_y^i \end{bmatrix}=\begin{bmatrix} q(\vec{r}) & w(\vec{r}) \\ w(\vec{r}) & p(\vec{r}) \end{bmatrix}\begin{bmatrix} f_x^j \\ f_y^j \end{bmatrix}. \tag{12}$$

Rather than inverting the large matrix with every pixel (x_i,y_i) relative to all other pixels (x_j,y_j), we calculated u_x^i and u_y^i separately at each pixel with a 10×10 pixel (500 m) window in order to save computational cost.

Just as for the damped least squares solution (Section 4.1), the degree to which we require the material to behave like an elastic solid will affect the resulting 3-D displacement field. Here, we append the matrix λ^* to the system matrix in Equation 8, where the optimal value for λ is again found using the *jRi* method (Barn-

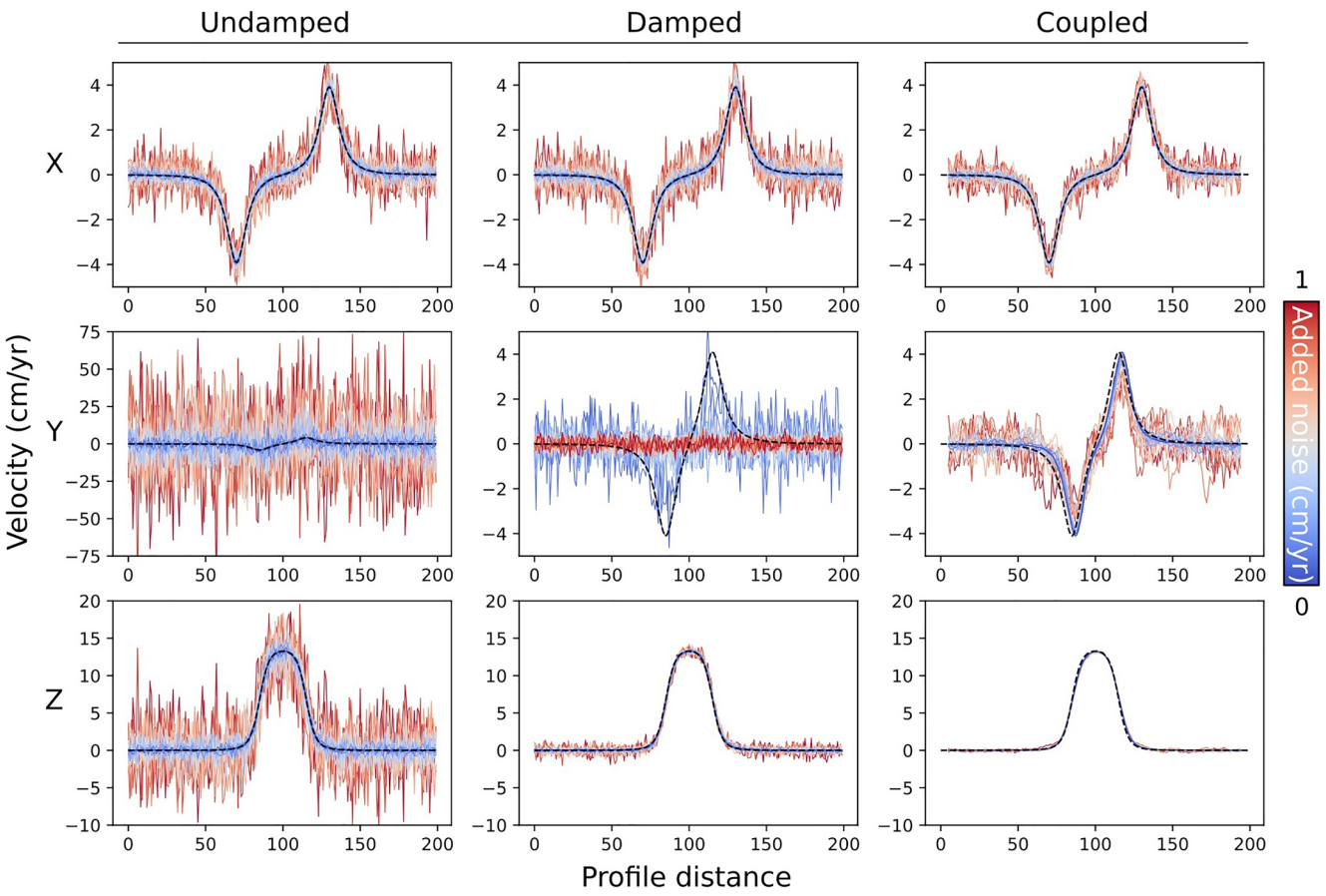

Figure 7. Inversions of synthetic data for 3-D surface velocity for the undamped, damped, and coupled cases. Curves are colored by noise level standard deviation (upto $\sigma = 1$) added to the synthetic line-of-sight images. Black dashed lines are the "true" velocities associated with the buried dislocation. Units are arbitrary, but are chosen to approximate the ~10 cm/yr line-of-sight (LOS) signals observed for the Whitewater basin data. Scales on *Y*-axis for the Y-velocities are allowed to vary between panels to emphasize the magnitude of variability associated with the various approaches.

hart & Lohman, 2010). It is also important to note here that displacements associated with discontinuities (e.g., faults that creep at the surface would violate the assumptions from Haines et al., 2015 and Sandwell & Wessel, 2016), so care should be taken with interpreting the results of this approach in those settings. As shown in the results below, there are no sharp discontinuities in the original LOS observations or 3-D decompositions that would indicate the presence of shallow creep. However, there are some residuals associated with the fit to the original LOS observations using the coupled approach (Figure S1) that indicate that this example may approach the limits of this assumption.

4.3. Synthetic Data Tests

In addition to applying these approaches to the data set covering the Whitewater sub-basin, we compared the results of each inversion method applied to synthetic data. This enabled us to assess the accuracy of the method and compare sensitivities to varying noise levels. We used a synthetic deformation scenario with a buried horizontal dislocation embedded in an elastic half space (Okada, 1985). The rectangular opening source has dimensions of 60 units in the X direction and 30 units in the Y direction centered in a 200-by-200 unit area, where units are arbitrary. We used the 3-D surface velocity associated with tensile faulting (opening perpendicular to the dislocation surface), projected along the four LOS vectors available for the Whitewater study region, as our synthetic data, with the magnitude of opening chosen so that the peak LOS deformation is 10 cm/yr. We added white noise drawn from a normal distribution with a range of magnitudes for each LOS observation. Noise levels consisted of a set of 60 increasing values ranging from a standard deviation of 0–1 cm/yr (Figures 7 and 8).

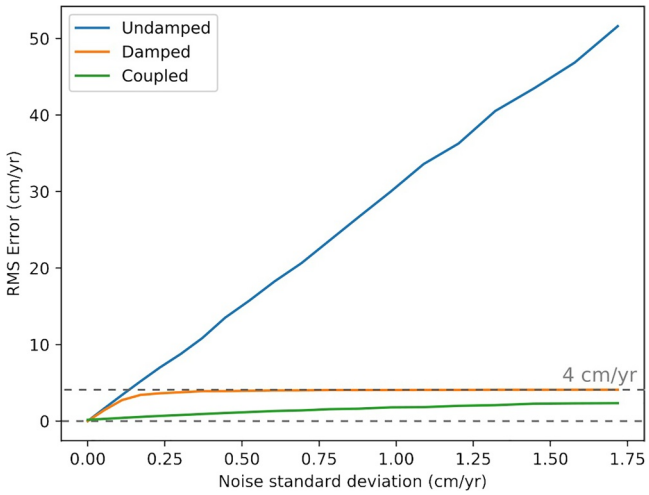

Figure 8. RMS error (computed from 1,000 realizations at each noise level) of the inferred north-south velocities from the undamped, damped, and coupled synthetic test cases taken from the location of peak velocity. The dashed 4 cm/yr line indicates the actual peak value of the input Y-velocity, indicating that most of the error in the damped solution comes from the over-damping toward zero.

We attempt to recover the 3-D velocities from the noisy LOS observations with three methods: (1) the undamped least squares inversion (Section 3), (2) the damped least squares inversion (Section 4.1), and (3) the elastically coupled inversion (Section 4.2). We show transects through the resulting displacement fields at their peaks to illustrate how the recovered 3-D displacements compare to the true synthetic signals (Figure 7). Values for the best-fit choice of λ based on the *jRi* method (Barnhart & Lohman, 2010) increase with increasing noise for the damped and coupled cases. The synthetic tests with the largest levels of noise actually have the smallest inferred Y-values for the damped case (middle panel, Figure 7), due to the larger value of λ.

5. Results and Discussion

5.1. Results From Synthetic Tests

If there is zero noise added to the synthetic data, we exactly recover the correct 3-D displacements with the undamped least squares inversion, as expected. However, due to the poor constraints on the north-south direction, the undamped solution for the Y component is highly unstable and gives poor results in the presence of even minimal noise (Figures 7 and 8). The damped solution results in less variability in the inferred Y component. However, the solution is strongly biased toward zero, even for low noise levels (Figures 7 and 8). We find the results for the Y component are improved in the coupled solution.

We selected this synthetic scenario because of the similarity to the expected deformation above an aquifer. However, the relative performance of the coupled versus damped inversions will depend on how closely the actual behavior of the material conforms to the assumptions made in design of the coupled problem. Cases with significant anelastic behavior, surface rupture, etc., would likely perform less well than the scenario shown here.

5.2. Results at Whitewater Sub-Basin

The damped, undamped + UAVSAR and coupled inversions all are similar in terms of the inferred X and Z component of deformation (Figure 9). The undamped inversion that includes both UAVSAR and sentinel data (left column, Figure 9), has the greatest diversity of LOS directions, and results in a smoothly varying inferred Y-component of velocity, with peak magnitudes of around 6 cm/yr. The inferred Y-component is, as expected, most noisy for the damped inversion of only Sentinel-1 data (middle column, Figure 9), which has little sensitivity to northward displacement. The results for the coupled inversion have similar but slightly smaller magnitudes of Y-velocity than the undamped + UAVSAR model.

The profile A–A′, shown in Figure 10, also illustrates the similarity between inferred X and Z components of velocity for all models. The coupled model performs slightly better than the damped model in terms of the similarity to the inferred Y-component of velocity constrained by UAVSAR observations. Forward predictions of these 3D velocity fields into the LOS for each of the four available Sentinel tracks (including P173, which was not used in the analysis) and UAVSAR track can be found in supplemental Figure S1. Small, but spatially coherent residuals are associated with the coupled model in the regions with the highest strain rate gradients. This suggests that while there are no sharp discontinuities in the vicinity of the Garnet Hill fault present in the data, the assumptions about smooth signals used in our approach (Haines et al., 2015; Sandwell & Wessel, 2016) may not be entirely valid here. However, also note that this misfit to the Sentinel-1 observations is accompanied by a corresponding improvement in the fit to the UAVSAR data compared to the damped inversion. Because the UAVSAR data has the strongest constraints on the Y-component of velocity, the close correspondence of the coupled inversion results to the UAVSAR constraints supports its potential utility as an alternative approach to damping for regularization. More drastic improvements were

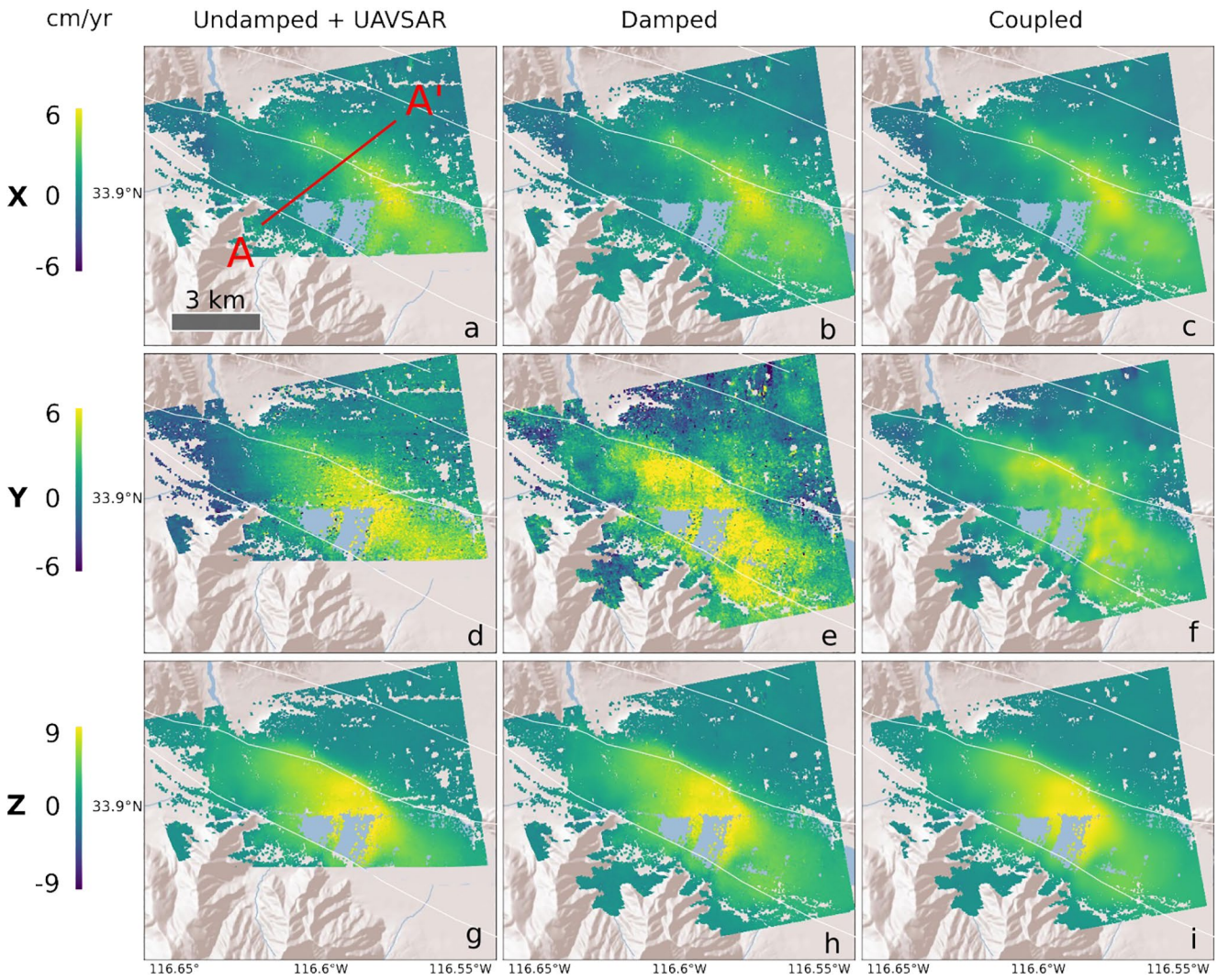

Figure 9. Results from inversion of multiple line-of-sight (LOS) values for X, Y, and Z velocity (Rows 1, 2, and 3, respectively). The time period is approximately from 02/2017–12/2017. Values are saturated outside of the range −6–+6 cm/yr for horizontal velocities and −9 – +9 cm/yr for vertical velocities. (Column 1) Inversion of data from three Sentinel-1 tracks and Uninhabited Aerial Vehicle Synthetic Aperture Radar (UAVSAR) with no damping. (Column 2) Inversion of only Sentinel-1 data with damping of the Y term. (Column 3) Inversion of only Sentinel-1 data with the elastically coupled inversion method. Red line in panel (a) indicates location of cross section in Figure 10. UCERF model has been removed from each component prior to each inversion to reduce the contribution from large-scale tectonic signals.

obtained using the coupled solution for the synthetic tests above (Figure 7) where our elasticity requirements were perfectly met.

5.3. Implications for Faults

Both mapped faults bounding the Whitewater sub-basin (the Garnet Hill fault to the north, and the Palm Springs blind fault to the south) appear to act as moderate barriers to groundwater flow, but the Garnet Hill fault shows a stronger strain gradient (Figures 3 and 4). The Palm Springs blind fault forms the boundary between basin sediments in the Coachella Valley, and crystalline basement rocks to the south. The Palm Springs blind fault also is located at the edge of the extent of good-quality InSAR data, with data quality decreasing rapidly due to the higher topographic relief in the south, so we do not interpret the signals across this fault. The Garnet Hill fault runs down the central portion of the valley, offsetting alluvium at shallow depths. The peak gradient that we observe in our data does not follow the mapped fault exactly, but diverges

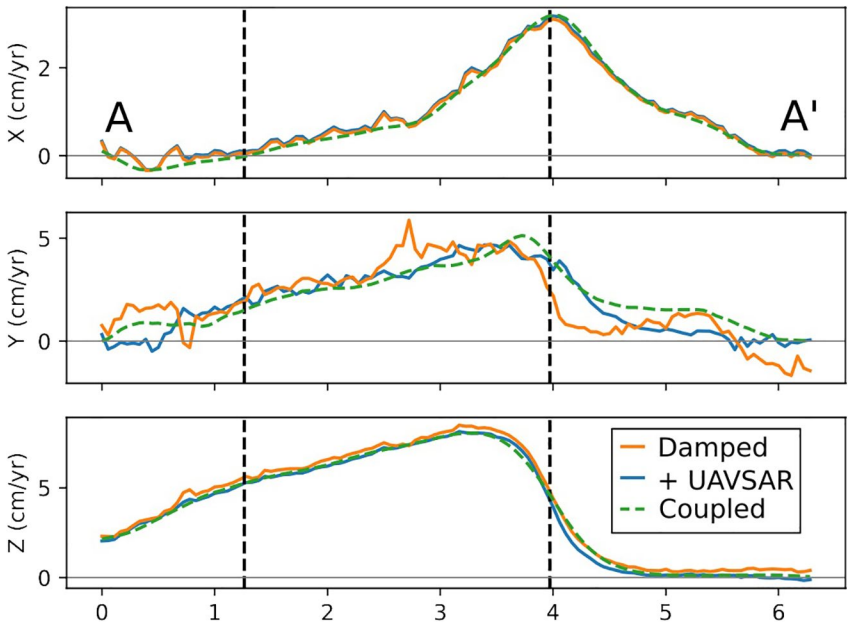

Figure 10. Cross sections (from red line in Figure 9a) of inferred 3-D velocities in 2017, with the damped Sentinel-1 inversion (orange), Sentinel-1 and Uninhabited Aerial Vehicle Synthetic Aperture Radar (UAVSAR) combined inversion (blue), and the coupled inversion of Sentinel-1 data (green).

to the northeast near the northwestern portion of our study area (Figures 3 and 4). This may represent the location of an unmapped fault that branches from the Garnet Hill fault, or perhaps an inaccuracy in the location of the mapped fault. Alternatively, the asymmetrical surface deformation pattern across the fault may be related to factors such as an irregularly dipping fault geometry or variations in permeability along the fault.

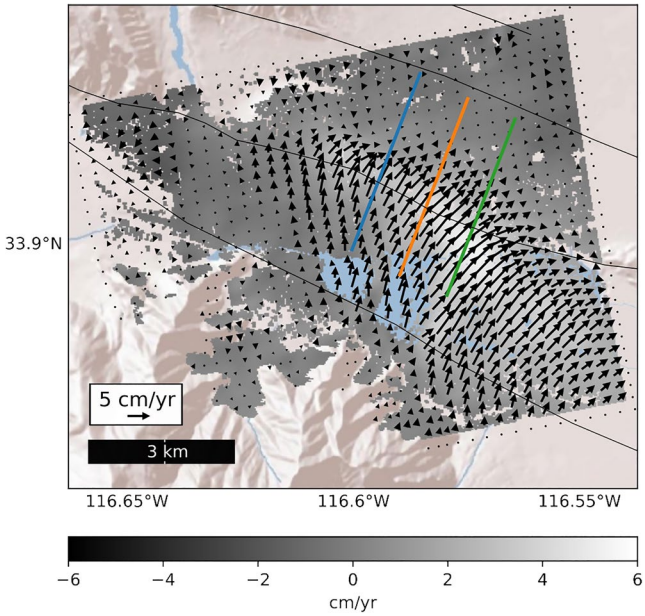

Figure 11. Average velocities in 2017 from coupled inversion, including vertical (gray-scale saturated at 6 cm/yr), and horizontal velocities (black vectors) derived from the coupled solution. Colored lines show location of profiles shown in Figure 12.

We focus on gradients in velocity across and along the fault rather than the absolute magnitudes to avoid any dependence on the method we use to determine our reference frame. Strong gradients are concentrated near the Garnet Hill fault (Figures 9–12), which can be seen clearly in the fault-parallel and fault-perpendicular components of velocity along three separate profiles (Figures 11 and 12). Profiles in Figure 12 illustrate how these components of strain vary as the profiles cross the fault from the southwest to the northeast. The northwestern-most profile (blue) crosses the fault in the vicinity of the peak difference in location between the mapped fault trace and the strongest gradient in LOS velocity.

The along-fault gradients vary between the northwestern-most profile (blue lines, Figures 11 and 12) and southeastern-most profile (green lines, Figures 11 and 12). Note that, for all three inversion approaches, fault-parallel displacement (top row, Figure 12) along the blue profile (northwestern-most profile) shows an increase in the degree of right-lateral strain as the profile crosses the fault, while a slight decrease in right-lateral strain is present in the southeast (green line). The largest increase in right-lateral strain along the blue profile occurs to the northeast of the Garnet Hill fault, in the vicinity of the potentially unmapped fault described in the previous section.

The fault-perpendicular velocity profiles (second row, Figure 12) show more similarity between the profiles, all show an overall decrease in fault-perpendicular (northeastward) velocity across the profile, suggest-

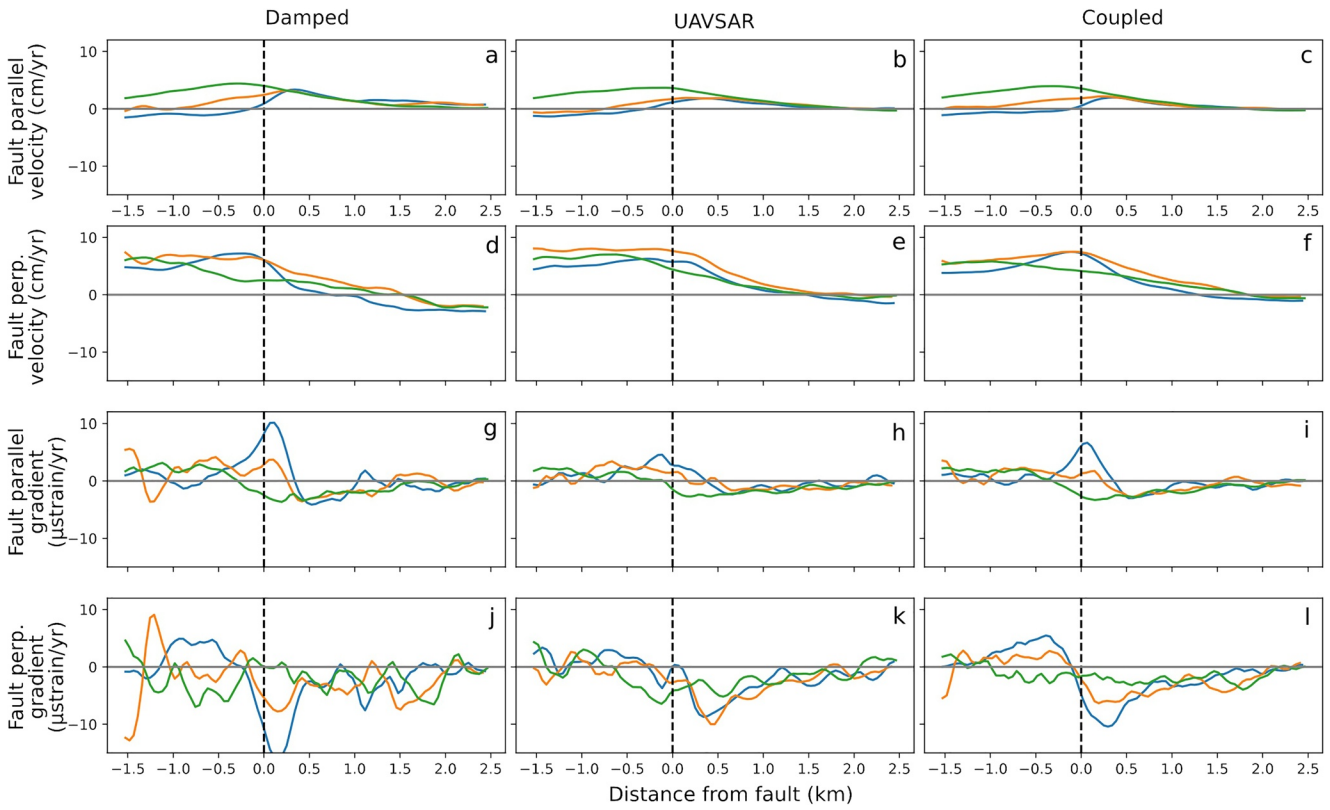

Figure 12. SW-NE fault-parallel (a–c) and fault-perpendicular (d–f) velocity profiles from Figure 11 relative to the Garnet Hill fault along with their respective gradients (g–i, right-lateral sense of strain is positive, (j–l), compression across the fault is negative). Profiles from damped, Uninhabited Aerial Vehicle Synthetic Aperture Radar (UAVSAR), and coupled inversions are shown for comparison. Location of the Garnet Hill fault is indicated by vertical black dashed lines in each panel. Damped and UAVSAR were filtered with a 6 pixel (~0.25 km) moving average to match the additional smoothing necessary to implement the coupled inversion. Interseismic motion has been removed using the UCERF model.

ing a slight contraction across the fault. In general, all three methods suggest that there is an increase in right-lateral strain in the vicinity of the blue profile, and that fault-perpendicular strain associated with the 2017 event would tend to place the fault under greater compression.

6. Conclusion

We have presented a method for regularizing inversions for 3-D displacements or velocities that includes constraints that couple the horizontal components of deformation. This results in an end-member model of 3D displacements that may be more physically realistic than those resulting from inversions that damp or ignore the north-south component of deformation. This end member may not be valid in cases where the deformation field includes discontinuities, such as those associated with faults creeping at shallow depth or landslides. This method can be particularly useful when data constraining north-south motion (e.g., UAVSAR) is noisy or simply does not exist for a particular area or time range. We compare our approach against other regularization methods for synthetic data, and find that, as expected, the undamped and damped least squares inversion for 3-D deformation fields result in poor resolution of the north-south component of deformation. The coupled inversion approach reproduces the input Y-component of deformation much more reliably in our synthetic scenarios, at least in this case where the underlying deformation field is smooth and is driven by elastic behavior.

While many applications may not require constraints on the N-S component of displacement, we show an example for the NW-SE-trending Garnet Hill fault in the Coachella Valley, where the values of the N-S component could have significant implications for the inferred state of stress along the shallow portions of the fault. For the Whitewater basin, we find that the damped and coupled approaches agree with the joint

UAVSAR-Sentinel inversion in terms of the major details in the velocity gradients near the Garnet Hill Fault. The agreement between the coupled and UAVSAR-Sentinel inversions suggests that the coupled approach could be a useful end member to consider in analyses of InSAR data where the underlying physical model is poorly understood. If the two solutions differed, then that would suggest that further analysis of physical models incorporating anelastic behavior or more careful consideration of the temporal variability between tracks was warranted.

Data Availability Statement

Sentinel-1a/b imagery is produced by the European Space Agency (ESA) and can be downloaded from the Alaska Satellite Facility (ASF) through the NASA Earth Science Data and Information System (ESDIS) project. Shuttle Radar Topography Mission (SRTM) digital elevation models can be downloaded through the United States Geological Survey (USGS). The authors acquired UAVSAR interferograms from NASA-JPL (Hensley et al., 2009). Data products discussed in this study, including LOS rates and the inversion results are included as supplemental files with this manuscript. Sentinel-1 data from Alaska Satellite Facility (ASF; vertex.daac.asf.alaska.edu), Sentinel-1 data, groundwater delivery data from the Coachella Valley Water District (CVWD; http://www.cvwd.org/), and well-based measurements of groundwater elevations from the United States Geological Survey (USGS; https://waterdata.usgs.gov).

Acknowledgments
The authors thank the National Aeronautics and Space Administration (NASA) (grants NNX16AL20G and NNX16AK57G) and the National Science Foundation (NSF) (grant EAR1949073) for funding this project, the European Space Agency (ESA) for acquiring Sentinel-1 data, Alaska Satellite Facility (ASF; vertex.daac.asf.alaska.edu) for archiving and providing Sentinel-1 data, the Coachella Valley Water District (CVWD; http://www.cvwd.org/) for providing groundwater delivery data, and the United States Geological Survey (USGS; https://waterdata.usgs.gov) for providing well-based measurements of groundwater elevations. Finally, they thank Eric Lindsey and one anonymous reviewer for their thoughtful review of this manuscript which greatly improved its quality.

References

Barnhart, W., & Lohman, R. (2010). Automated fault model discretization for inversions for coseismic slip distributions. *Journal of Geophysical Research*, *115*. https://doi.org/10.1029/2010jb007545

Bechor, N. B., & Zebker, H. A. (2006). Measuring two-dimensional movements using a single InSAR pair. *Geophysical Research Letters*, *33*. https://doi.org/10.1029/2006gl026883

Bürgmann, R., Rosen, P. A., & Fielding, E. J. (2000). Synthetic aperture radar interferometry to measure earth's surface topography and its deformation. *Annual Review of Earth and Planetary Sciences*, *28*, 169–209. https://doi.org/10.1146/annurev.earth.28.1.169

Caricchi, L., Annen, C., Blundy, J., Simpson, G., & Pinel, V. (2014). Frequency and magnitude of volcanic eruptions controlled by magma injection and buoyancy. *Nature Geoscience*, *7*, 126–130. https://doi.org/10.1038/ngeo2041

Chester, F. M., & Chester, J. S. (2000). Stress and deformation along wavy frictional faults. *Journal of Geophysical Research*, *105*, 23421–23430. https://doi.org/10.1029/2000jb900241

Delbridge, B. G., Bürgmann, R., Fielding, E., Hensley, S., & Schulz, W. H. (2016). Three-dimensional surface deformation derived from airborne interferometric UAVSAR: Application to the Slumgullion landslide. *Journal of Geophysical Research: Solid Earth*, *121*, 3951–3977. https://doi.org/10.1002/2015jb012559

De Zan, F., & Monti Guarnieri, A. (2006). TOPSAR: Terrain observation by progressive scans. *IEEE Transactions on Geoscience and Remote Sensing*, *44*, 2352–2360. https://doi.org/10.1109/tgrs.2006.873853

District, C. V. W. (2019). *{ENGINEER}'{S} {REPORT} {ON} {WATER} {SUPPLY} {AND} {REPLENISHMENT} {ASSESSMENT} Tech. Rep.)*. Coachella, CA: Coachella Valley Water District.

Ellsworth, W. L. (2013). Injection-induced earthquakes. *Science*, *341*. https://doi.org/10.1126/science.1225942

Farr, T. G., & Kobrick, M. (2000). Shuttle radar topography mission produces a wealth of data. *Eos, Transactions American Geophysical Union*, *81*, 583–585. https://doi.org/10.1029/eo081i048p00583

Fattahi, H., Agram, P., & Simons, M. (2016). A network-based enhanced spectral diversity approach for TOPS time-series analysis. *IEEE Transactions on Geoscience and Remote Sensing*, *55*, 777–786. https://doi.org/10.1109/TGRS.2016.2614925

Fialko, Y. (2004). Evidence of fluid-filled upper crust from observations of postseismic deformation due to the 1992 mw7. 3 landers earthquake. *Journal of Geophysical Research*, *109*. https://doi.org/10.1029/2004jb002985

Fialko, Y., Sandwell, D., Simons, M., & Rosen, P. (2005). Three-dimensional deformation caused by the bam, iran, earthquake and the origin of shallow slip deficit. *Nature*, *435*, 295–299. https://doi.org/10.1038/nature03425

Fialko, Y., Simons, M., & Agnew, D. (2001). The complete (3-D) surface displacement field in the epicentral area of the 1999MW7.1 Hector Mine Earthquake, California, from space geodetic observations. *Geophysical Research Letters*, *28*, 3063–3066. https://doi.org/10.1029/2001gl013174

Froger, J.-L., Fukushima, Y., Briole, P., Staudacher, T., Souriot, T., & Villeneuve, N. (2004). The deformation field of the August 2003 eruption at Piton de la Fournaise, Reunion Island, mapped by ASAR interferometry. *Geophysical Research Letters*, *31*. https://doi.org/10.1029/2004gl020479

Funning, G. J., Parsons, B., Wright, T. J., Jackson, J. A., & Fielding, E. J. (2005). Surface displacements and source parameters of the 2003 Bam (Iran) earthquake from Envisat advanced synthetic aperture radar imagery. *Journal of Geophysical Research*, *110*. https://doi.org/10.1029/2004jb003338

González, P. J., Tiampo, K. F., Palano, M., Cannavó, F., & Fernández, J. (2012). The 2011 lorca earthquake slip distribution controlled by groundwater crustal unloading. *Nature Geoscience*, *5*, 821–825. https://doi.org/10.1038/ngeo1610

Grandin, R., Klein, E., Métois, M., & Vigny, C. (2016). Three-dimensional displacement field of the 2015Mw8.3 Illapel earthquake (Chile) from across- and along-track Sentinel-1 TOPS interferometry. *Geophysical Research Letters*, *43*, 2552–2561. https://doi.org/10.1002/2016gl067954

Gray, L. (2011). Using multiple RADARSAT InSAR pairs to estimate a full three-dimensional solution for glacial ice movement. *Geophysical Research Letters*, *38*. https://doi.org/10.1029/2010gl046484

Haines, A. J., Dimitrova, L. L., Wallace, L. M., & Williams, C. A. (2015). *Enhanced surface imaging of crustal deformation: Obtaining tectonic force fields using GPS data* (p. 99). Springer. https://doi.org/10.1007/978-3-319-21578-5

Handwerger, A. L., Fielding, E. J., Huang, M.-H., Bennett, G. L., Liang, C., & Schulz, W. H. (2019). Widespread initiation, reactivation, and acceleration of landslides in the northern California Coast Ranges due to extreme rainfall. *Journal of Geophysical Research*, *124*, 1782–1797. https://doi.org/10.1029/2019JF005035

Hanssen, R. F. (2001). *Radar interferometry: Data interpretation and error analysis* (p. 308). Springer Science & Business Media.

Hearn, E. H., & Bürgmann, R. (2005). The effect of elastic layering on inversions of gps data for coseismic slip and resulting stress changes: Strike-slip earthquakes. *Bulletin of the Seismological Society of America*, *95*, 1637–1653. https://doi.org/10.1785/0120040158

Hensley, S., Zebker, H., Jones, C., Michel, T., Muellerschoen, R., & Chapman, B. (2009). First deformation results using the NASA/JPL UAVSAR instrument. In *2009 2nd Asian-pacific conference on synthetic aperture radar* (pp. 1051–1055). https://doi.org/10.1109/APSAR.2009.5374246

Hu, J., Li, Z.-W., Sun, Q., Zhu, J.-J., & Ding, X.-L. (2012). Three-dimensional surface displacements from InSAR and GPS measurements with variance component estimation. *IEEE Geoscience and Remote Sensing Letters*, *9*, 754–758. https://doi.org/10.1109/LGRS.2011.2181154

Hu, J., Li, Z.-W., Zhu, J., Ren, X., & Ding, X. (2010). Inferring three-dimensional surface displacement field by combining SAR interferometric phase and amplitude information of ascending and descending orbits. *Science China Earth Sciences*, *53*, 550–560. https://doi.org/10.1007/s11430-010-0023-1

Hu, X., & Bürgmann, R. (2020). Aquifer deformation and active faulting in Salt Lake Valley, Utah, USA. *Earth and Planetary Science Letters*, *547*, 116471. https://doi.org/10.1016/j.epsl.2020.116471

Jiang, H., Feng, G., Wang, T., & Bürgmann, R. (2017). Toward full exploitation of coherent and incoherent information in Sentinel-1 TOPS data for retrieving surface displacement: Application to the 2016 Kumamoto (Japan) earthquake. *Geophysical Research Letters*, *44*, 1758–1767. https://doi.org/10.1002/2016GL072253

Johnson, C. W., Fu, Y., & Bürgmann, R. (2017). Seasonal water storage, stress modulation, and California seismicity. *Science*, *356*, 1161–1164. https://doi.org/10.1126/science.aak9547

Jónsson, S., Zebker, H., Segall, P., & Amelung, F. (2002). Fault slip distribution of the 1999 Mw 7.1 hector mine, California, earthquake, estimated from satellite radar and GPS measurements. *Bulletin of the Seismological Society of America*, *92*(4), 1377–1389. https://doi.org/10.1785/0120000922

Joughin, I. R., Kwok, R., & Fahnestock, M. A. (1998). Interferometric estimation of three-dimensional ice-flow using ascending and descending passes. *IEEE Transactions on Geoscience and Remote Sensing*, *36*, 25–37. https://doi.org/10.1109/36.655315

Jung, H.-S., Lu, Z., & Zhang, L. (2012). Feasibility of along-track displacement measurement from sentinel-1 interferometric wide-swath mode. *IEEE Transactions on Geoscience and Remote Sensing*, *51*, 573–578. https://doi.org/10.1109/TGRS.2012.2197861

Keranen, K. M., & Weingarten, M. (2018). Induced seismicity. *Annual Review of Earth and Planetary Sciences*. *46*, 149–174. https://doi.org/10.1146/annurev-earth-082517-010054

Lindsey, E. O., Fialko, Y., Bock, Y., Sandwell, D. T., & Bilham, R. (2014). Localized and distributed creep along the southern San Andreas Fault. *Journal of Geophysical Research: Solid Earth*, *119*, 7909–7922. https://doi.org/10.1002/2014jb011275

Menke, W. (2018). *Geophysical data analysis: Discrete inverse theory* (p. 352). Academic press.

Michel, R., Avouac, J.-P., & Taboury, J. (1999). Measuring ground displacements from SAR amplitude images: Application to the Landers earthquake. *Geophysical Research Letters*, *26*, 875–878. https://doi.org/10.1029/1999gl900138

Murray, K. D., & Lohman, R. B. (2018). Short-lived pause in Central California subsidence after heavy winter precipitation of 2017. *Science Advances*, *4*, eaar8144. https://doi.org/10.1126/sciadv.aar8144

Okada, Y. (1985). Surface deformation due to shear and tensile faults in a half-space. *Bulletin of the Seismological Society of America*, *75*, 1135–1154.

Parsons, T., Johnson, K. M., Bird, P., Bormann, J., Dawson, T. E., Field, E. H., et al. (2013). *Appendix C—Deformation models for UCERF3*. online. https://doi.org/10.1093/oxfordhb/9780199556939.013.0016

Rosen, P. A., Gurrola, E., Sacco, G. F., & Zebker, H. (2012). The InSAR scientific computing environment. In *EUSAR 2012; 9th European conference on synthetic aperture radar* (pp. 730–733). Nuremberg, Germany.

Rosen, P. A., Hensley, S., Wheeler, K., Sadowy, G., Miller, T., Shaffer, S., et al. (2006). UAVSAR: A new NASA airborne SAR system for science and technology research. In *2006 IEEE conference on radar* (p. 8). https://doi.org/10.1109/RADAR.2006.1631770

Ross, Z. E., Cochran, E. S., Trugman, D. T., & Smith, J. D. (2020). 3D fault architecture controls the dynamism of earthquake swarms. *Science*, *368*, 1357–1361. https://doi.org/10.1126/science.abb0779

Samieie-Esfahany, S., Hanssen, R., van Thienen-Visser, K., & Muntendam-Bos, A. (2009). On the effect of horizontal deformation on InSAR subsidence estimates. In *Proceedings of the Fringe 2009 workshop*. Frascati, Italy (*30*, p. 7).

Sandwell, D. T., & Wessel, P. (2016). Interpolation of 2-D vector data using constraints from elasticity. *Geophysical Research Letters*, *43*, 10–703. https://doi.org/10.1002/2016gl070340

Savage, H. M., Kirkpatrick, J. D., Mori, J. J., Brodsky, E. E., Ellsworth, W. L., Carpenter, B. M., et al. (2017). Scientific exploration of induced seismicity and stress (SEISMS). *Scientific Drilling*, *23*, 57–63. https://doi.org/10.5194/sd-23-57-2017

Segall, P. (1989). Earthquakes triggered by fluid extraction. *Geology*, *17*, 942–946. https://doi.org/10.1130/0091-7613(1989)017<0942:etbfe>2.3.co;2

Simons, M., Fialko, Y., & Rivera, L. (2002). Coseismic Deformation from the 1999 Mw 7.1 Hector Mine, California, Earthquake as Inferred from InSAR and GPS Observations. *Bulletin of the Seismological Society of America*, *92*(4), 1390–1402. https://doi.org/10.1785/0120000933

Wetzler, N., Shalev, E., Göbel, T., Amelung, F., Kurzon, I., Lyakhovsky, V., & Brodsky, E. E. (2019). Earthquake swarms triggered by groundwater extraction near the dead sea fault. *Geophysical Research Letters*, *46*, 8056–8063. https://doi.org/10.1029/2019gl083491

Wright, T. J., Parsons, B. E., & Lu, Z. (2004). Toward mapping surface deformation in three dimensions using InSAR. *Geophysical Research Letters*, *31*. https://doi.org/10.1029/2003gl018827